Available online at www.sciencedirect.com
ScienceDirect
International Journal of Multiphase Flow 34 (2008) 408–418
International Journal of Multiphase Flow
www.elsevier.com/locate/ijmulflow

Gravity-driven motion of a deformable drop or bubble near an inclined plane at low Reynolds number

Andrew J. Griggs, Alexander Z. Zinchenko, Robert H. Davis *

Department of Chemical and Biological Engineering, University of Colorado, Boulder, CO 80309-0424, United States

Received 29 January 2007; received in revised form 1 August 2007

Abstract

The creeping motion of a three-dimensional deformable drop or bubble in the vicinity of an inclined wall is investigated by dynamical simulations using a boundary-integral method. We examine the transient and steady velocities, shapes, and positions of a freely-suspended, non-wetting drop moving due to gravity as a function of the drop-to-medium viscosity ratio, λ, the wall inclination angle from horizontal, θ, and Bond number, B, the latter which gives the relative magnitude of the buoyancy to capillary forces. For fixed λ and θ, drops and bubbles show increasingly pronounced deformation in steady motion with increasing Bond number, and a continued elongation and the possible onset of breakup are observed for sufficiently large Bond numbers. Unexpectedly, viscous drops maintain smaller separations and deform more than bubbles in steady motion at fixed Bond number over a large range of inclination angles. The steady velocities of drops (made dimensionless by the settling velocity of an isolated spherical drop) increase with increasing Bond number for intermediate-to-large inclination angles (i.e. $45° \leqslant \theta \leqslant 75°$). However, the steady drop velocity is not always an increasing function of Bond number for viscous drops at smaller inclination angles.

1. Introduction

The motion of a deformable drop through a viscous liquid near an inclined plane wall is studied here as a function of the drop-to-medium viscosity ratio λ, wall inclination angle θ (from horizontal), and Bond number, $B = \Delta\rho g a^2/\sigma$, where $\Delta\rho$ is the density difference between the drop and suspending medium, a is the non-deformed spherical radius of the drop, g is the acceleration due to gravity, and σ is the interfacial tension. It is assumed that the drop does not wet the wall; rather, it remains separated from the wall by a layer of the suspending liquid.

The existing literature addressing the motion of deformable drops or bubbles near an inclined wall or in inclined channels includes both experimental and theoretical studies for small and large Reynolds numbers. For example, Mortazavi and Tryggvason (2000) used level-set and front-tracking methods to study the motion of a drop in a channel at moderate Reynolds number. Tsao and Koch (1997) considered high-Reynolds-number motion of a bubble moving perpendicular or parallel to an inclined wall. Even though the Reynolds numbers used in their experiments are not small ($Re = 40$–300, based on the settling velocity of a sphere and the drop radius), they recognized that viscous forces, rather than inertial forces, beneath the drop are capable of balancing the gravitational force normal to the plane wall. For small Reynolds number (Stokes flow), boundary-integral methods, such as the one used in the current work, provide for efficient and highly accurate tracking of a deformable interface, even for very small drop-to-wall separations. DeBisschop et al. (2002) used a boundary-integral method to study the Stokes motion of a 2D homoviscous droplet confined between two walls under gravity, with and without the presence of surfactant, as a function of Bond number and inclination angle. Although ranges of Bond number and inclination angles were explored by DeBisschop et al. (2002), the presented results are limited to $\lambda = 1$, and the important case of small inclination angles and Bond numbers was not considered.

* Corresponding author.
E-mail address: robert.davis@colorado.edu (R.H. Davis).

0301-9322/$ - see front matter © 2007 Elsevier Ltd. All rights reserved.
doi:10.1016/j.ijmultiphaseflow.2007.10.006

The motion of a spherical drop parallel to a plane wall, corresponding to $B \to 0$, has been examined computationally for small Reynolds number by Chen and Keh (2001) as a function of viscosity ratio and distance from the wall, using a boundary-collocation technique. When the component of gravity normal to the wall is nonzero, a spherical drop will asymptotically approach the wall and not reach a steady separation and velocity.

The low-Reynolds-number motion of a deformable drop near an inclined plane wall was also considered by Hodges et al. (2004), for somewhat restrictive conditions (e.g., small tilt angle relative to horizontal). Provided that B was not too large ($B \ll \theta^{-1}$ in two dimensions and $B \ll \theta^{-4/3}$ in three dimensions, with θ in radians), they used (i) a capillary-static approximation for the drop shape away from the wall, (ii) lubrication theory for the thin film between the drop and the wall, and (iii) a combination of lubrication theory and half-plane boundary-integral calculation for the drop interior. While the two-dimensional results presented in their work cover a wide-range of parameter space, the three-dimensional results presented are less comprehensive. This type of method is essentially asymptotic and typically predicts drop velocities with logarithmic accuracy. Finding the range of validity for these approximations would require full boundary-integral simulations or comparison with experiments. The calculations from Hodges et al. (2004) predict greater velocities than experimental measurements of Aussillous and Quere (2002) for bubbles moving near an inclined wall, but show qualitative agreement with experimental results for small inclination angles (e.g., 5.6°).

To provide accurate predictions for a deformable drop near an inclined plane wall over wide parameter ranges, the present work explores the (B, λ, θ)-parameter space for $Re \ll 1$ using full three-dimensional boundary-integral simulations. Although small and large drop deformations are studied here, we consider primarily subcritical Bond numbers, for which drop breakup does not occur. Steady-state and transient quantities such as gap thickness, drop shapes, and velocities are provided. The principal computational difficulties are for small inclination angles, which include the long time required to reach a steady state, coupled with the fact that the stable choice of time step depends proportionately on the minimum mesh spacing, and a large number of elements on the drop surface are required for sufficient numerical resolution. The boundary-integral algorithm is similar to that of Griggs et al. (2006) for drop motion in a channel with two parallel walls, and uses the Green's function for the half-space adjacent to an infinite plane wall, which circumvents discretization of the wall and is capable of better accuracy and computational speed.

2. Boundary-integral formulation

We consider the motion of a deformable drop near a wall inclined at angle θ (relative to horizontal), under creeping flow conditions. Both the drop and external suspending fluids are considered Newtonian, and have densities ρ_d and ρ_e and viscosities μ_d and μ_e, respectively. The system is assumed isothermal and devoid of surfactants, so that the interfacial tension is constant. For any point on the drop surface, S, the interfacial velocity, $\mathbf{u}(\mathbf{y})$, satisfies the boundary-integral equation for a deformable interface (Rallison and Acrivos, 1978):

$$u^k(\mathbf{y}) = 2\kappa \int_S \mathbf{u}(\mathbf{x}) \cdot \boldsymbol{\tau}^k(\mathbf{x};\mathbf{y}) \cdot \mathbf{n}(\mathbf{x}) \mathrm{d}S_{\mathbf{x}} + F^k(\mathbf{y}), \tag{1}$$

$$F^k(\mathbf{y}) = \frac{2}{(\lambda+1)} \frac{1}{\mu_e} \int_S f(\mathbf{x}) \mathbf{n}(\mathbf{x}) \cdot \mathbf{G}^k(\mathbf{x};\mathbf{y}) \mathrm{d}S_{\mathbf{x}}, \tag{2}$$

where $\mathbf{G}^k(\mathbf{x};\mathbf{y})$ is the Green's function for the half-space above an infinite plane wall, i.e. the Stokes velocity generated at $\mathbf{x}$ by the unit point force applied to $\mathbf{y}$ along the kth Cartesian coordinate axis ($k = 1, 2, 3$). The stress tensor corresponding to the fundamental solution, $\mathbf{G}^k(\mathbf{x};\mathbf{y})$, is $\boldsymbol{\tau}^k(\mathbf{x};\mathbf{y})$, $\mathbf{n}(\mathbf{x})$ is the unit normal pointing from the drop interface into the surrounding fluid, the drop-to-medium viscosity ratio is $\lambda = \mu_d/\mu_e$, and $\kappa = (\lambda - 1)/(\lambda + 1)$. Finally, $f(\mathbf{x}) = 2\sigma k(\mathbf{x}) - \Delta\rho_{\mathbf{g}} \cdot \mathbf{x}$, so that $f(\mathbf{x})\mathbf{n}(\mathbf{x})$ is the stress jump across the interface due to the assumed constant interfacial tension, σ, and the buoyancy force due to gravity, with $\Delta\rho = |\rho_d - \rho_e|$ and $\mathbf{g}$ being the gravitational acceleration, and $k(\mathbf{x}) = \frac{1}{2}(k_1 + k_2)$ is the local mean curvature at $\mathbf{x}$. The Cartesian coordinate system x_1, x_2, x_3 is chosen such that the plane $x_3 = 0$ serves as the bounding wall, as shown in Fig. 1.

The marginal eigenvalues ($\kappa = \pm 1$) of (1) can be purged through Wielandt deflation (Kim and Karrila, 1991), resulting in substantial improvements to convergence of the iterative solutions for $\lambda \ll 1$ or $\lambda \gg 1$. The deflated form of the boundary-integral equation is given by

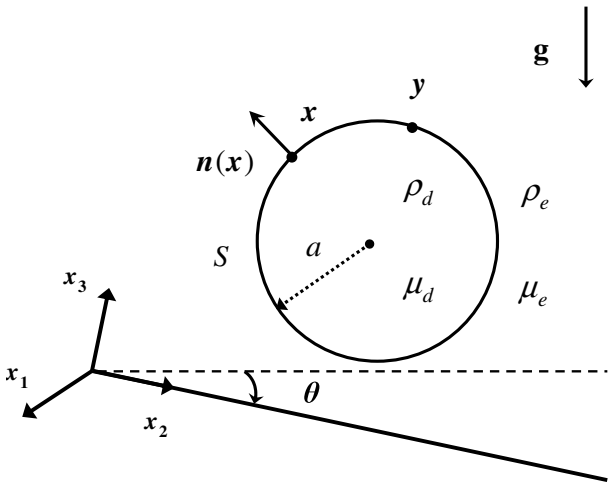

Fig. 1. Geometry of an initially spherical drop near an inclined wall.

$$w_k(\mathbf{y}) = \kappa\left[2\int_S \mathbf{w}(\mathbf{x})\cdot\boldsymbol{\tau}^k(\mathbf{x};\mathbf{y})\cdot\mathbf{n}(\mathbf{x})\mathrm{d}S_{\mathbf{x}} - w'_k(\mathbf{y}) + \frac{n_k(\mathbf{y})}{S}\int_S \mathbf{w}(\mathbf{x})\cdot\mathbf{n}(\mathbf{x})\mathrm{d}S_{\mathbf{x}}\right] + F^k(\mathbf{y}), \quad (3)$$

for $\mathbf{w} = \mathbf{u} - \kappa\mathbf{u}'$, where the prime denotes the projection of a vector field on the space of rigid-body motions, and

$$\mathbf{u} = \mathbf{w} - \frac{\kappa}{1-\kappa}\mathbf{w}'. \quad (4)$$

Following singularity and near-singularity subtraction, (3) becomes suitable for efficient numerical solutions. The field $\mathbf{w}'(\mathbf{y})$ can be calculated, without Gram–Schmidt orthogonalization, as in Zinchenko et al. (1997).

3. Numerical method

The Green's function for the whole half-space $x_3 > 0$, which satisfies the no-slip boundary condition on the wall, can be represented as the sum of the free-space and wall-correction parts (i.e., $\mathbf{G}(\mathbf{x};\mathbf{y}) = \mathbf{G}_0(\mathbf{x}-\mathbf{y}) + \mathbf{G}^l_W(\mathbf{x};\mathbf{y})$) and was originally derived by Blake (1971). Advantages of using this Green's function in the boundary-integral method include that discretization of the bounding wall is not required, instead only the drop surface must be discretized, and the resulting second-kind integral equation is suitable for iterative solution by successive substitutions (Kim and Karilla, 1991).

The free-space term is the fundamental solution for the velocity in an unbounded fluid,

$$\mathbf{G}^k_0(\mathbf{x}-\mathbf{y}) = -\frac{1}{8\pi}\left[\frac{\mathbf{e}_k}{r} + \frac{r_k\mathbf{r}}{r^3}\right], \quad (5)$$

with $\mathbf{r} = \mathbf{x} - \mathbf{y}$ and $r = \|\mathbf{r}\|$. The wall-correction part is

$$\mathbf{G}^k_W(\mathbf{x};\mathbf{y}) = -\frac{1}{8\pi}\left[-\left(\frac{\mathbf{e}_k}{r} + \frac{r_k\mathbf{r}}{r^3}\right) + m\left\{2y_3(y_3 - r_3)\left(\frac{\mathbf{e}_k}{r^3} - 3\frac{r_k\mathbf{r}}{r^5}\right) - 2y_3\left(\frac{\delta_{k3}\mathbf{r} - r_k\mathbf{e}_3}{r^3}\right)\right\}\right], \quad (6)$$

where $r = \|\mathbf{r}\| = \|\mathbf{x} - \mathbf{y}^{\mathrm{IM}}\|$, $\mathbf{y}^{\mathrm{IM}}$ is the mirror image of the point $\mathbf{y}$ with respect to the wall, and $m = \pm 1$, with the plus sign for $k = 1, 2$ and minus sign for $k = 3$. The singularity for the wall-correction Green's function lies outside the domain at $\mathbf{x} = \mathbf{y}^{\mathrm{IM}}$.

The standard second-order Runge–Kutta method is used to update the interface. The choice of time step is similar to that employed for two drops in close approach (Zinchenko and Davis, 2005) and ensures adequate stability for calculations of drops in close proximity to the bounding walls. To avoid difficulties with mesh degradation in dynamical simulations, "passive" mesh stabilization techniques are employed to maintain the quality of surface triangulation with fixed topology as time proceeds. The essence of this procedure is to construct an additional global tangential field on the drop surface from the solution of a variational problem. Since most of our simulations involve moderate-to-large deformations, a curvature-adaptive version of passive mesh stabilization is used, as described by Eqs. (5.3)–(5.6) of Zinchenko et al. (1999). Although the deflated system (3) has suitable spectral properties for simple iterations, the speed of convergence may be slow for extreme viscosity ratios and small drop-to-wall spacings. To expedite calculations, a version of the generalized minimal–residual method is used as in Zinchenko and Davis (2000), which alleviates the observed slow convergence of simple iterations, especially for low viscosity ratios.

4. Results

For the results presented here, the length and the velocity scales are, respectively, the non-deformed spherical drop radius, a, and the settling velocity of an isolated spherical drop:

$$U_{\mathrm{S}} = \frac{2}{9}\frac{(\lambda+1)}{(\lambda+2/3)}\frac{\Delta\rho g a^2}{\mu_{\mathrm{e}}}, \quad (7)$$

where g is the magnitude of acceleration due to gravity. At the start of simulations, the drop shape is spherical and positioned above the inclined wall. It is assumed here that $\rho_{\mathrm{d}} > \rho_{\mathrm{e}}$, so that the drop sediments down the wall, although the solution also applies to $\rho_{\mathrm{d}} < \rho_{\mathrm{e}}$, where the drop rises along the wall. Numerical results are presented as functions of the Bond number, $B = \Delta\rho g a^2/\sigma$, which is a measure of the relative magnitude of gravitational to interfacial forces, the drop-to-medium viscosity ratio, λ, and inclination angle, θ. Drop velocities are defined as the average fluid velocity over the drop volume and is calculated using Gauss theorem (Griggs et al., 2006; Zinchenko and Davis, 2006). The distance between the drop and the wall is expressed as the minimum gap, δ, which is calculated as the distance between closest triangle vertex and the wall.

4.1. Intermediate-to-large inclination angles

The simulation results for intermediate-to-large inclination angles (i.e., $45° \leqslant \theta \leqslant 75°$) are nearly insensitive to the level of triangulation explored for these inclination angles, except for a few extreme cases (e.g., largely deformable drops and nearly spherical drops moving close to the wall). For cases when the drop does not deform appreciably or approaches the wall closely (e.g., within 1% of the drop radius), using only a moderate number of triangles, typically $N_\triangle = 3840$ and 6000, provides sufficient numerical resolution, although the results reported here are for $N_\triangle = 8640$ triangles, unless otherwise noted. In this section, drop motion is studied first for an inclination angle of $\theta = 60°$, where several prominent physical phenomena are revealed, and then selected results are shown for other angles.

First, we consider the effect of varying the Bond number, while the viscosity ratio and tilt angle are fixed. Results for $\theta = 60°$ and $\lambda = 1$ are shown in Fig. 2, where plots of

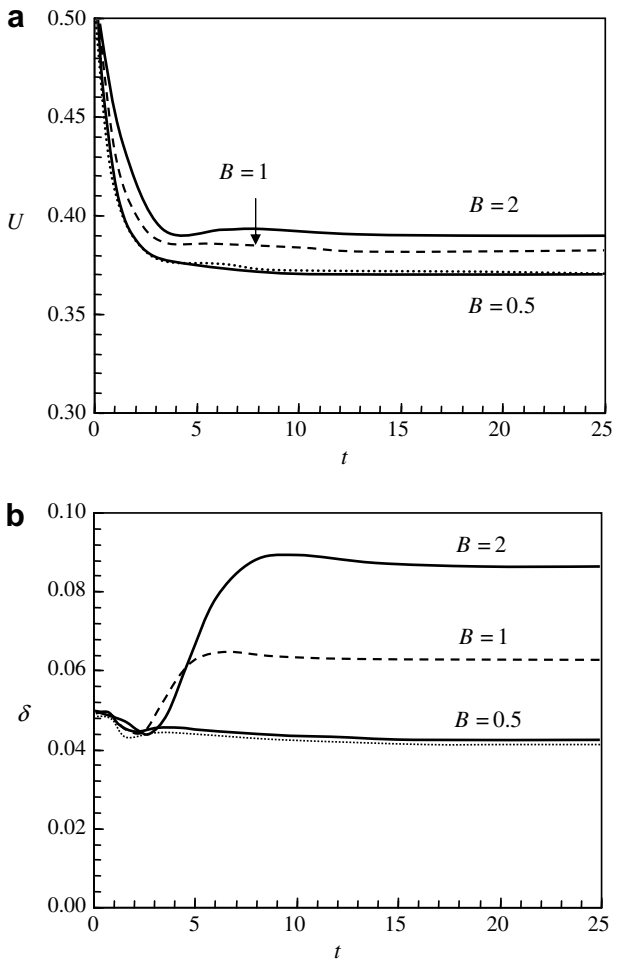

Fig. 2. Simulation results for $N_{\triangle} = 8640$, $\theta = 60°$, and $\lambda = 1$ showing (a) the velocity and (b) minimum gap with time over a range of Bond numbers. The dotted lines represent calculations performed using $N_{\triangle} = 3840$.

the drop velocity parallel to the wall, U, and the minimum gap distance, δ, as functions of time are given, for a range of $B = 0.5$–2.0 using $N_{\triangle} = 8640$. Simulation results for a lower triangulation level, $N_{\triangle} = 3840$, have been included in Fig. 2 as the dotted line for the most challenging case of $B = 0.5$. The lower resolution gives almost identical results as the higher resolution, except for the minimum gap during part of the transient period. Here, the drop shape is initially spherical, with an initial drop-to-wall separation of $0.05a$. Following an initial period of deformation, during which the minimum gap decreases, the drop moves either towards or away from the wall, depending on B, and eventually reaches a steady shape and velocity. For Bond numbers greater than 0.7, the steady drop-to-wall separation increases from its initial value, while for smaller B, a decrease from the initial value is observed. During the initial period as the drop approaches the wall, viscous forces in the fluid layer between the drop and the wall, in concert with gravitational forces, act to deform the drop, giving rise to some interesting dynamical behavior. For example, the drop with $B = 2$ initially approaches the wall more closely than does the drop with $B = 0.5$ (see Fig. 2b, at $t \sim 3.5$). This result can be attributed to elongation of the drop along the x_2-axis and the subsequent development of a tail, which is very close to the wall. With time, interfacial forces cause the tail to retract and the drop moves away from the wall, reaching a steady position, shape, and velocity, as depicted in Fig. 3. As shown in Fig. 2a, the steady velocity increases with increasing B, which is most likely related to the larger steady distance from the wall for larger B. Since gravitational forces act to deform the drop from its initial spherical shape, we anticipate increasingly pronounced deformation with increasing Bond number. Fig. 4 shows steady drop shapes

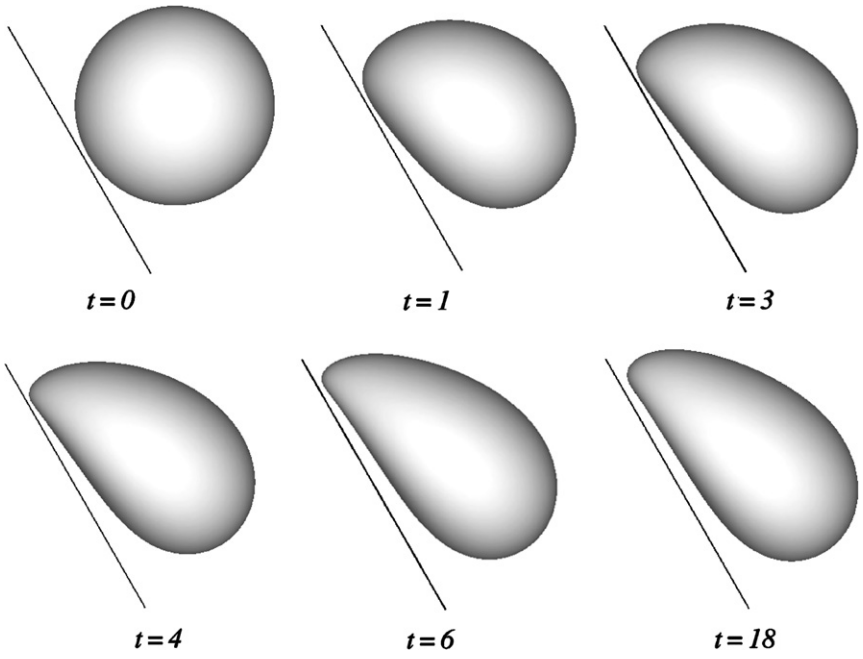

Fig. 3. Evolution of drop shape with time for $\theta = 60°$, $\lambda = 1$, and $B = 2$.

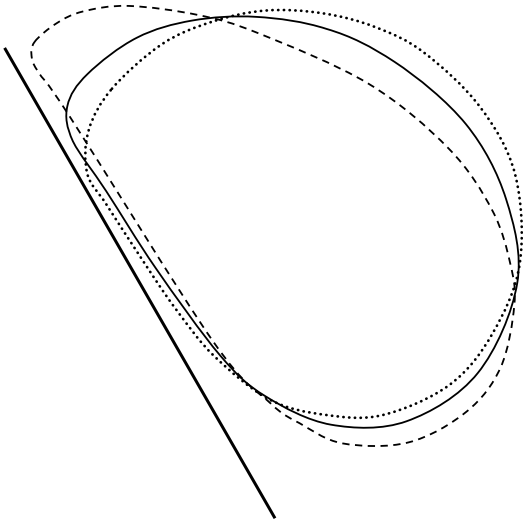

Fig. 4. Steady drop shapes shown as cross-sections in the plane of symmetry ($x_1 = 0$) for $\theta = 60°$, $\lambda = 1$, and $B = 2.0$ (dashed), 1.0 (solid), and 0.5 (dotted).

(shown here as stacked contours in the plane $x_1 = 0$) for the same conditions as in Fig. 2, where the expected trends are evident. These simulation results are in qualitative agreement with the two-dimensional study from DeBisschop et al. (2002) for the gravity-driven motion of a drop in an inclined channel.

We now consider the effect of varying the viscosity ratio, for $\theta = 60°$ and $B = 2$. Results for the translational velocity and the minimum drop-to-wall spacing are plotted versus dimensionless time in Fig. 5. Here, viscous drops move closer to the wall in steady motion than do bubbles ($\lambda = 0$). The most viscous drop ($\lambda = 5$) shows similar dynamic behavior when compared to the homoviscous drop ($\lambda = 1$), as described above, except that it settles slower and closer to the wall. Simulation results for a lower triangulation level, $N_\triangle = 3840$, have been included in Fig. 5 as the dotted line for the case $\lambda = 5$, with the lower resolution giving identical results as the higher triangulation, except for the minimum gap during part of the initial transient period. The inviscid bubble ($\lambda = 0$) migrates rapidly away from the wall and reaches a steady velocity and shape faster than do the drops. By fixing B, the ratio of gravitational and interfacial forces is constant, and differences in physical behavior with varying viscosity ratio are directly related to the viscous forces in the fluid layer between the drop and wall. These viscous forces play an increasingly dominant role in influencing the overall drop motion as λ increases, as evidenced by the steady drop velocities in Fig. 5a. Steady drop shapes are given in Fig. 6. With increasing λ, the drops become increasingly deformed, similar to earlier work on drop deformations in linear flows (Stone et al., 1986). However, the minimum gap for the more deformed drop is less, in contrast to the observations for fixed λ, where larger Bond numbers gave rise to larger steady minimum gaps, deformations, and velocities.

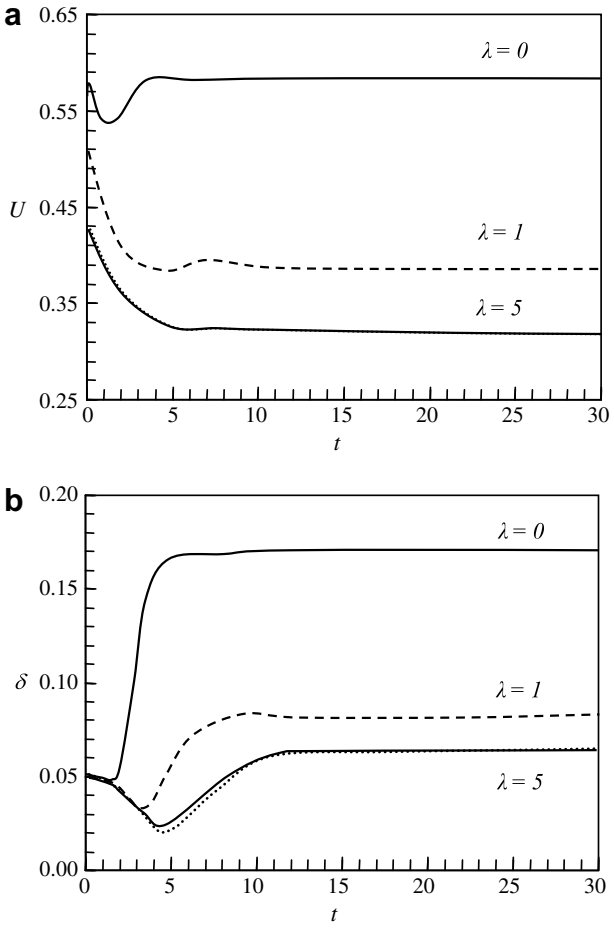

Fig. 5. Simulation results for $N_\triangle = 8640$, $\theta = 60°$, and $B = 2$ showing (a) the velocity and (b) minimum gap with time over a range viscosity ratios. The dotted lines represent calculations performed using $N_\triangle = 3840$.

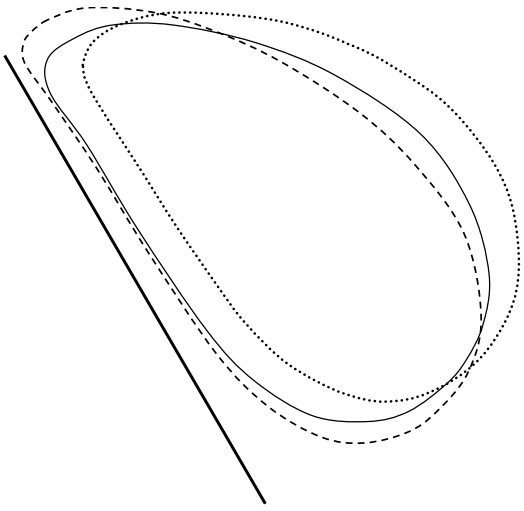

Fig. 6. Steady drop shapes shown as cross-sections in the plane of symmetry ($x_1 = 0$) for $\theta = 60°$, $B = 2$, and viscosity ratios $\lambda = 0$ (dotted), 1 (solid), and 5 (dashed).

For the motion of viscous drops near an inclined wall at large-to-intermediate angles, steady shapes and velocities may not exist. Our boundary-integral results indicate that,

for sufficiently large Bond numbers and viscosity ratios, the drops continuously elongate, possibly approaching breakup. Fig. 7 compares the drop elongation (relative to the non-deformed spherical diameter, and calculated as the maximum distance between mesh points), E, and the minimum gap for drops over a wide-range of viscosity ratios with $B = 2.5$ and $\theta = 60°$. The initial stages for all viscosity ratios are similar: the drop deforms from its initial spherical shape and the tail approaches the wall closely, although the rate of elongation in the initial stages depends on the viscosity ratio. For $\lambda = 0$ and $\lambda = 1$, the tail retracts and a steady shape, position, and velocity are eventually reached (see Figs. 5 and 6). In contrast, for $\lambda = 10$, the body of the drop moves away from the wall, while the tail approaches the wall, resulting in the continual elongation. For $\lambda = 1$, continual elongation is observed for Bond numbers above 3 for $\theta = 60°$. In contrast, we do not observe such continual elongation for bubbles ($\lambda = 0$), even for Bond numbers as large as 5, at this inclination angle. A more complete study of the critical conditions for steady behavior, versus continual elongation and possible breakup, will be the subject of later work. The focus of the current study is on the behavior of drops and bubbles under sub-critical conditions.

Fig. 8 shows the steady velocity and minimum gap as functions of the Bond number for an inclination angle of 60°. Here, the steady velocity has been divided by $\sin\theta$, so that the normalization is based on the component of the isolated drop velocity in the direction along the plane. The so-defined steady velocity and gap distance are increasing functions of Bond number and inclination angle for this region of parameter space, and are more sensitive for larger inclination angles. Here, the steady velocity and minimum gap are increasing functions of B over the range λ and B considered. The physical behavior for $\theta = 60°$ is also observed for other large inclination angles. For example, Fig. 9 summarizes the steady velocities and minimum gaps as functions of Bond number for inclination angles of $\theta = 45°$, 60°, and 75°, with $\lambda = 1$. Similar behavior occurs for $\lambda \neq 1$ (i.e., steady velocity and minimum gap are

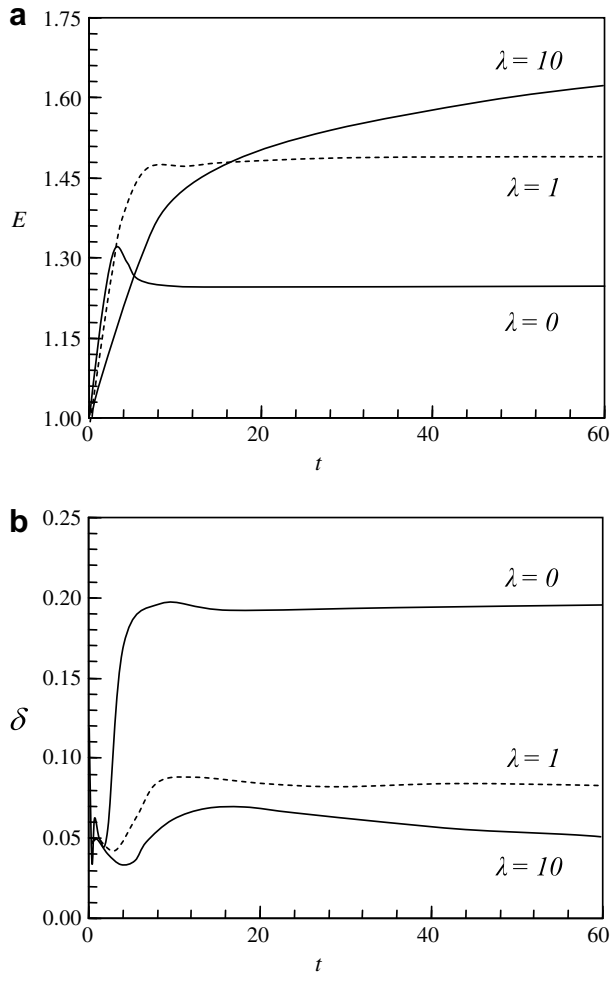

Fig. 7. Simulation results for $\theta = 60°$ and $B = 2.5$ showing (a) the maximum drop elongation and (b) minimum gap with time for a range of viscosity ratios.

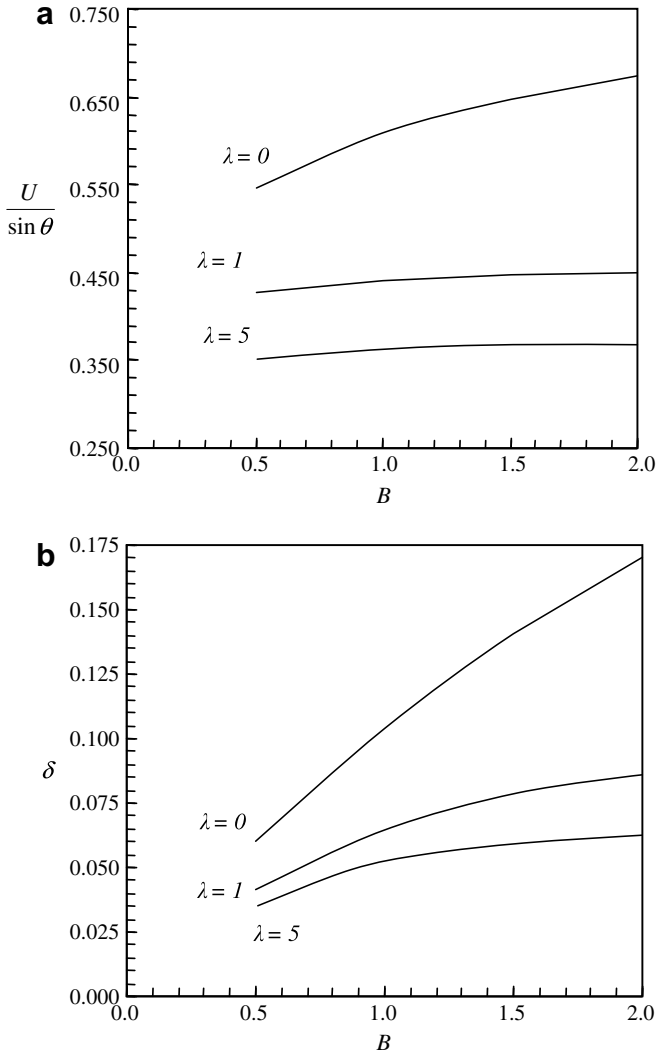

Fig. 8. Steady state (a) drop velocity and (b) minimum gap as a functions of Bond number and viscosity ratio for $\theta = 60°$.

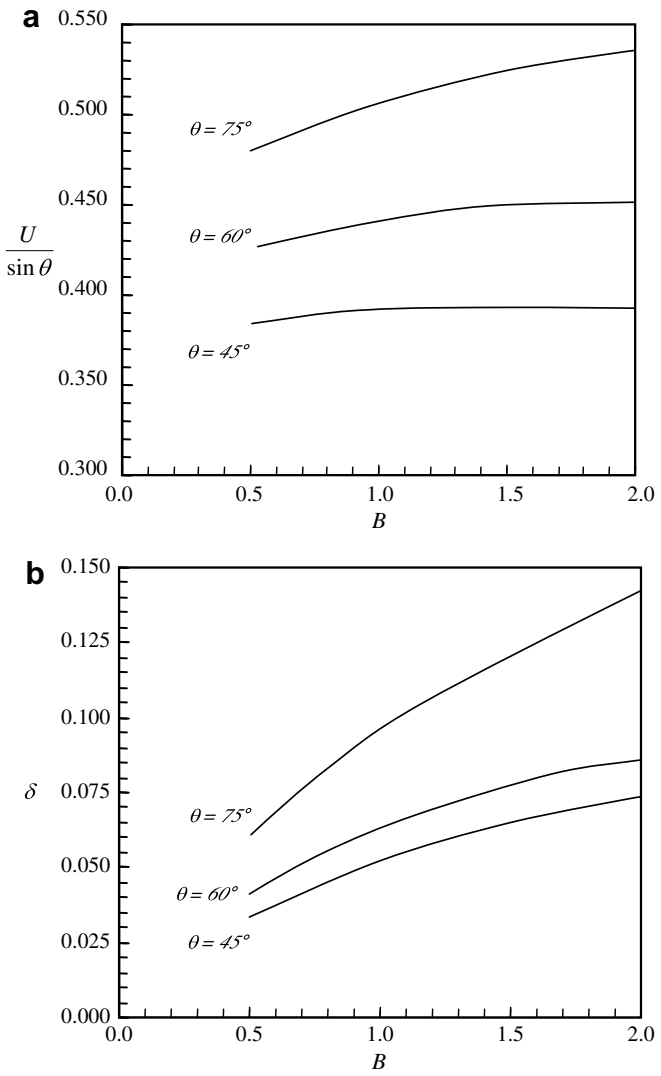

Fig. 9. Steady state (a) drop velocity and (b) minimum gap as a functions of Bond number and inclination angle for $\lambda = 1$.

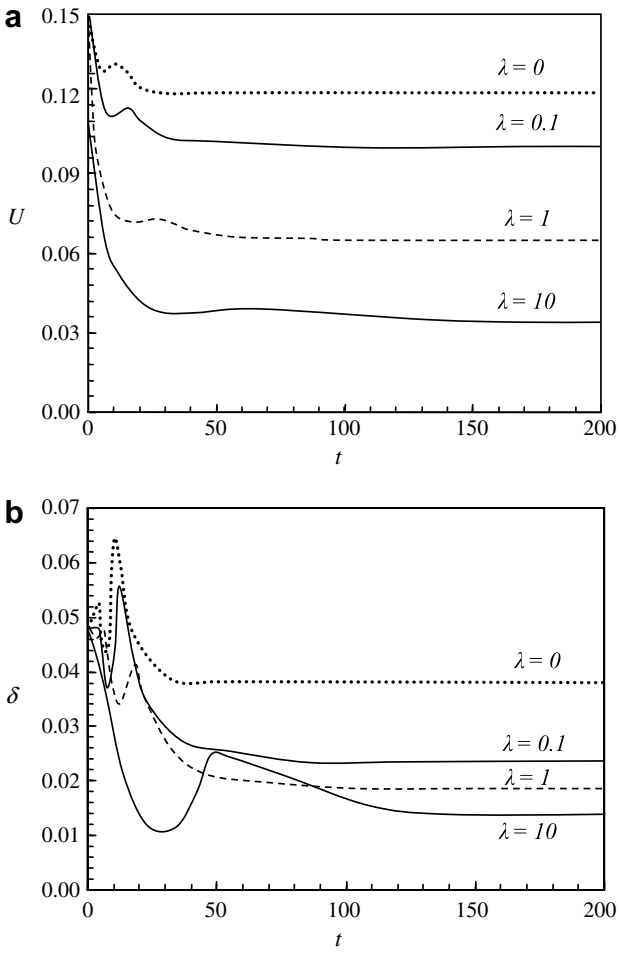

Fig. 10. Simulation results for $\theta = 15°$ and $B = 3$ showing the (a) drop velocity and (b) minimum gap with time over a range of viscosity ratios.

increasing functions of B) over the range θ and B considered in Fig. 9, although the onset of impending breakup is expected to depend on both B and λ. In the next section, we consider smaller inclination angles, where very different trends are observed than those for intermediate-to-large angles.

4.2. Small inclination angles

Smaller inclination angles present several computational challenges, as well as some interesting physical behaviors. First, drops and bubbles move closer to the wall at smaller angles than for higher angles, due to the greater normal component of gravity, which necessitates higher levels of triangulation (e.g., $N_{\triangle} = 8640$ instead of $N_{\triangle} = 3840$ to obtain accurate steady shapes and velocities). Second, the time needed to reach a steady state increases, due to this close approach and the smaller tangential component of gravity moving the drop or bubble along the wall, which results in a greater number of required time steps. For example, a typical simulation for $\theta = 60°$ for $\lambda \neq 1$ takes only a few hours for the drop to reach a steady velocity and position, while for $\theta = 15°$ the same value of B and λ, the simulation can often take 1–2 days, using an AMD 2800+ under Visual Fortran. For $\lambda = 1$, the time requirements are several fold less, since the first term on the right-hand side of (1) drops out and iterations are not required. In this section, we show that, for sufficiently small angles, viscous drops do not continually elongate but instead reach steady shapes and velocities for all conditions examined. Also, in contrast to larger inclination angles, the steady velocity is not always an increasing function of Bond number.

We begin our examination for small inclination angles by considering in Fig. 10 the effect of varying the viscosity ratio with a fixed Bond number of $B = 3$ and an inclination of $\theta = 15°$. As with larger inclination angles, a bubble ($\lambda = 0$) reaches steady state faster, migrates further from the wall, and obtains a higher steady velocity than do the viscous drops, but these differences are more pronounced for the small inclination angle. The homoviscous drop ($\lambda = 1$) behaves almost like the highly viscous drop

($\lambda = 10$), and obtains a steady velocity and gap that are much closer to those for $\lambda = 10$ than to those for the bubble ($\lambda = 0$). Even a small amount of drop viscosity ($\lambda = 0.1$) causes substantial deviation from $\lambda = 0$.

Fig. 11 shows snapshots of the bottoms of the drops for the same conditions as Fig. 10 at time $t = 200$ (which is essentially the steady state), with shading to indicate the gap profiles (lighter shades are closer to the wall). Several important observations can be made regarding these profiles, which directly influence the overall drop motion. Clearly, the drop-to-wall clearance is not uniform over the near-contact region. For all of these cases, the steady drop shapes exhibit neither a discernable "flat spot" nor a simple "pancake" shape, but a rim or dimple is observed instead. The viscosity ratio has a large effect on the shape of the steady near-contact region. For the inviscid drop ($\lambda = 0$), the tail of the drop is closest to the wall, and the region near the wall can be described as a posterior rim. When the viscosity ratio is increased to $\lambda = 1$, a noticeable dimple forms. The highly viscous drop ($\lambda = 10$) in Fig. 11 not only has a smaller minimum gap, but a larger portion of the drop surface is closer to the wall. Here, a very pronounced dimple has formed and, when compared with the $\lambda = 1$ case, the drop seems to have spread radially outward, rather than just being stretched in the direction of descent. The difference in the minimum gaps for $\lambda = 1$ and $\lambda = 10$ drops is small, compared to the much larger minimum gap for the inviscid drop. To provide a more quantitative view, the gap profile for $\lambda = 10$ is represented using contour mapping in Fig. 12. Here, the separation distance from the wall for several level lines are given. The steady state shapes, shown as stacked slices in the plane $x_1 = 0$, for $\lambda = 10$, 1, and 0 are shown in Fig. 13. It is interesting to note that the viscous drop is not as elongated (or stretched) along the direction of the wall as the homoviscous drop. The asymptotic analysis of Hodges et al. (2004) does not attempt to resolve the shape of the drop near the wall, but instead the drop shape is prescribed as either spherical, spherical with a flat spot, or pancake shaped. The complex shapes observed here show that

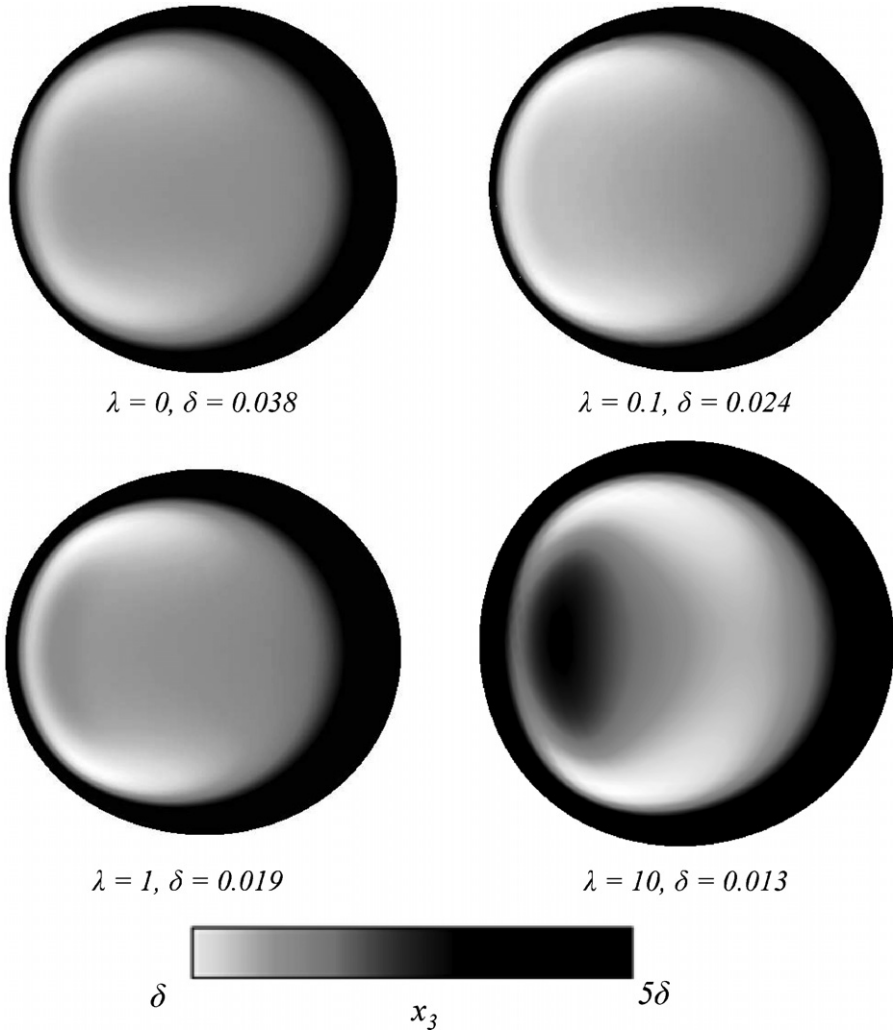

Fig. 11. Simulation results for $\theta = 15°$ and $B = 3$ showing the shape of the bottom of the drop near the wall; the direction of the drop motion is to the right.

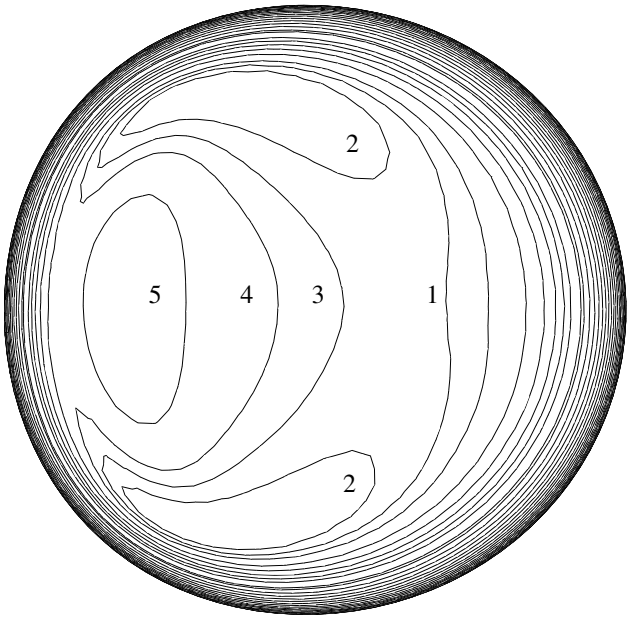

Fig. 12. Contour map showing the distance of the bottom of the drop interface from the wall for x_3 (1) 0.025, (2) 0.020, (3) 0.025, (4) 0.030, and (5) 0.040 for $\theta = 15°$, $B = 3$, and $\lambda = 10$. The additional contours are increase in increments of 0.005 x_3.

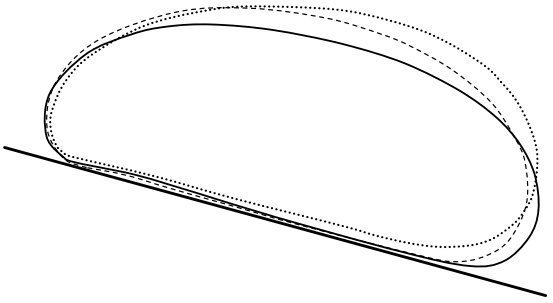

Fig. 13. Steady drop shapes shown as cross-sections in the plane of symmetry ($x_1 = 0$) for $\theta = 15°$, $B = 3$, and viscosity ratios $\lambda = 0$ (dotted), 1 (solid), and 10 (dashed).

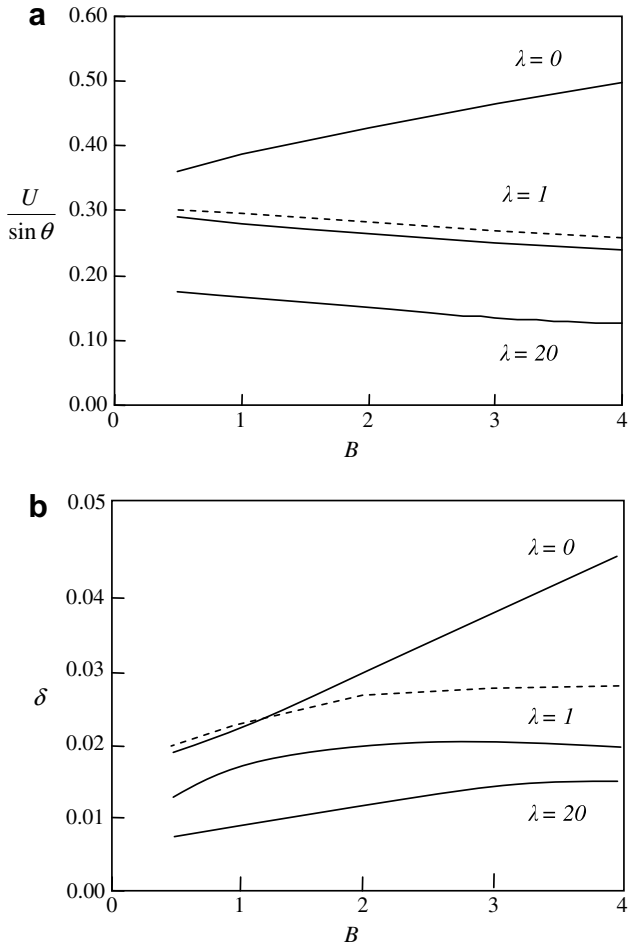

Fig. 14. Simulation results for the steady (a) drop velocity and (b) minimum gap for $\theta = 15°$ (solid lines) over a range of Bond numbers for different viscosity ratios; the dashed curves are for $\lambda = 1$ and $\theta = 20°$.

resolving the three-dimensional complicated shapes and the gap profiles are important in predicting the velocities of drops moving near an inclined wall.

The steady velocity and minimum gap as functions of Bond number and viscosity ratio are shown in Fig. 14 for an inclination angle of $\theta = 15°$, with $\theta = 20°$ included for $\lambda = 1$. For intermediate-to-large inclination angles, the steady velocity was found to be a monotonically increasing function of Bond number (see Figs. 2, 8, and 9). However, this generalization does not hold for small inclination angles. Although the steady velocity for bubbles ($\lambda = 0$) is an increasing function of Bond number, homoviscous drops ($\lambda = 1$) and highly viscous drops ($\lambda = 20$) exhibit decreasing steady velocities with increasing Bond number in the range examined. This contrast is surprising since, in both cases, the steady gap increases with Bond number. However, the drag is increased with increasing B by the drop elongation and complicated shape near the wall. In Fig. 15, we provide the gap profiles for the drop and bubble near the wall for $B = 0.5$ and 4 for the bubbles and highly viscous drops. From the above discussion on drop shape and its role in influencing drop motion, we know that the formation of a dimple is prevalent for viscous drops, but this feature is absent in bubbles. The presence of a dimple introduces a form of drag, since the fluid trapped in this region must be carried with the drop as it descends the wall. With increasing Bond number, the dimple becomes more prominent for viscous drops, which slows the drops down, as can represented in Fig. 16. Bubbles exhibit different physical behavior: a dimple does not form, but instead only a semi-circular rim near the tail, which grows in width with increasing Bond number, is observed. The effect of Bond number on drop deformation for small inclination angles is illustrated in Fig. 17, where the slices of the steady shapes for $\lambda = 1$ are given for $B = 4$, 2, and 0.5 are given. For the larger Bond numbers, the drop is stretched along the wall, whereas for the smaller Bond number, the bulk of the drop remains spherical, while the bottom has deformed in the region close to the wall.

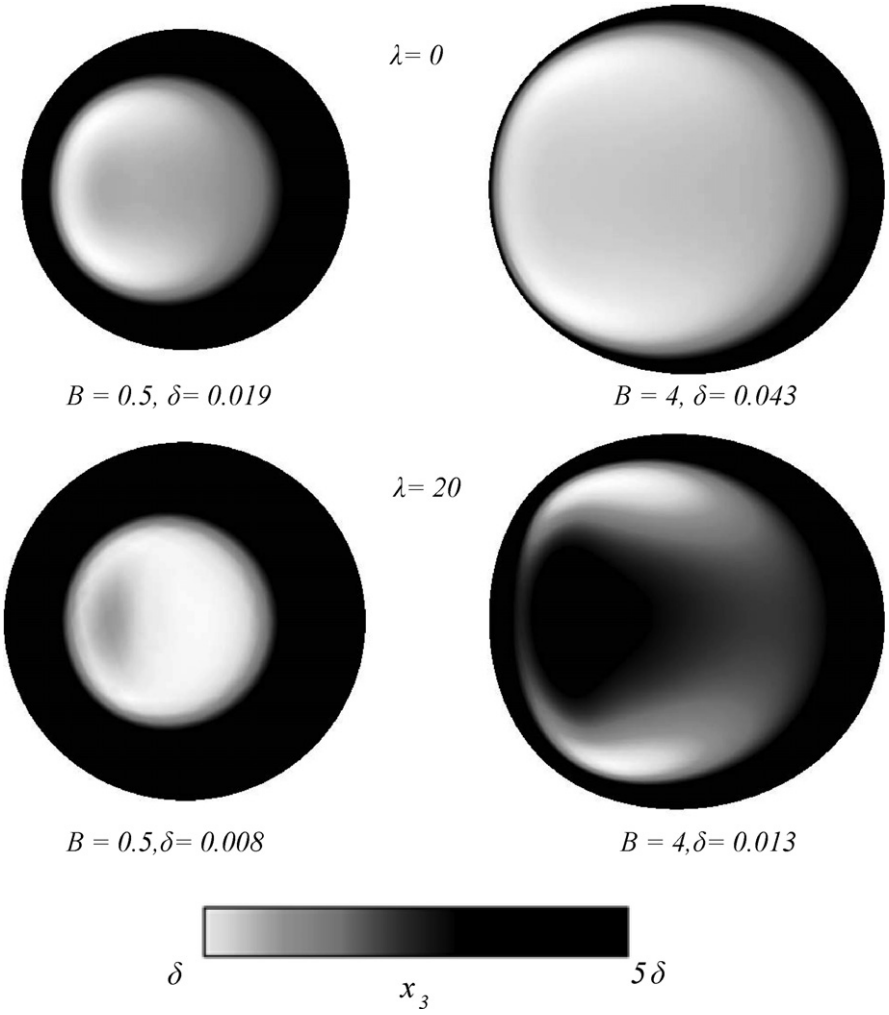

Fig. 15. Simulation results for $\theta = 15°$ comparing the shape of the bottom of the drop near the wall for a bubble and a viscous drop.

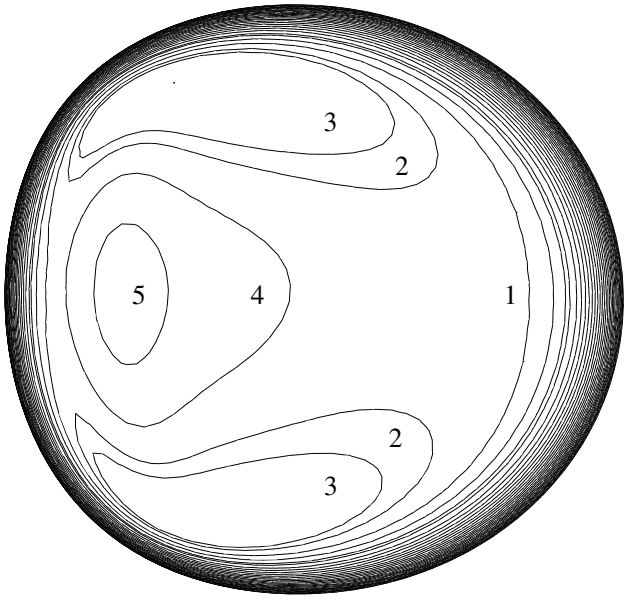

Fig. 16. Contour map showing the distance of the bottom of the drop interface from the wall for x_3 (1) 0.045, (2) 0.035, (3) 0.025, (4) 0.045, and (5) 0.055 for $\theta = 15°$, $B = 4$, and $\lambda = 20$. The additional contours are increase in increments of 0.005 x_3.

The trend of increasing steady velocity with increasing Bond number that we predict for bubbles is in agreement with the experimental work of Aussillous and Quere (2002), where the creeping motion of air bubbles under a tilted plate through viscous silicon oil was considered for small inclination angles. Moreover, Richard and Quere (1999) studied the motion of non-wetting glycerol droplets

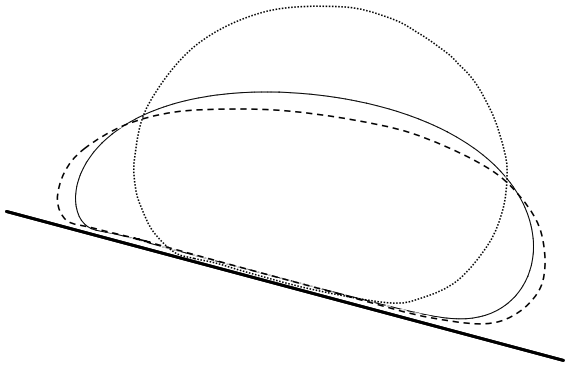

Fig. 17. Steady drop shapes shown as cross-sections in the plane of symmetry ($x_1 = 0$) for $\theta = 15°$, $\lambda = 1$, and $B = 4.0$ (dashed), 2.0 (solid), and 0.5 (dotted).

near a hydrophobically-modified plate in air and observed that the steady velocity decreases with increasing drop size for small inclination angles. Hodges et al. (2004) argue that the drop-to-medium viscosity ratio plays a dominant role in the types of motion for a drop moving near an inclined wall. For small λ, they predict the drop will "slip" down the plane, with external viscous stresses driving a passive recirculating flow in the drop interior, while for $\lambda \to \infty$ the drop will slide down the plane without rotating. For intermediate λ, they expect the drop to move in a combination of sliding, slipping, and rolling. These interesting physical phenomena provide motivation for additional experimental and computational work.

5. Concluding remarks

We have studied the low-Reynolds-number gravitational motion of a deformable drop or bubble through a viscous medium near an inclined plane wall as a function of the inclination angle, viscosity ratio, and Bond number. The steady non-dimensional velocity is an increasing function of B for large-to-intermediate inclination angles (i.e. $45° \leqslant \theta \leqslant 75°$) for the range of B considered, even though the deformation also increases with increases in B. This trend can be attributed to the position of the drop relative to the wall: drops with small Bond number approach the wall closely, and, as a result, experience more drag in the gap region and move slower than do drops with larger Bond number. For sufficiently high B, θ, and λ, the drops appear to exhibit continual elongation and do not approach a steady state. To follow this elongation with time, and possible breakup, would require greater triangulation and a modified mesh algorithm and can be the study of future work.

Compared with larger inclination angles, different physical behavior for drops and bubbles is predicted at smaller inclination angles. The scenario of impending drop breakup was not observed for small inclination angles, even when larger Bond numbers and viscosity ratios were considered. For fixed B and λ, the viscous forces in the region between the drop and the wall seem to play a more significant role for smaller inclination angles, which is evidenced by the complicated shape of the drop near the interface. Bubbles were observed to form a semi-circular rim near the tail that approaches the wall closely, while the front of the drop was elevated. The elevated front and semi-circular rim are not present in viscous drops; rather, the front, sides, and rear of the drop are more proximate to the walls and form a circular dimple, which becomes increasingly pronounced as the Bond number or viscosity ratio is increased, causing a decrease in the steady velocity. The predicted trend of decreasing velocity with increasing Bond number seen in Fig. 11 for viscous drops at small inclination angles is not expected to persist for very small Bond numbers, however, as then the drop will deform very little, approach the wall very closely, and slow down as a result.

Acknowledgements

This work was supported by the National Aeronautics and Space Administration and by the Petroleum Research Fund of the American Chemical Society. Andrew Griggs was also supported by a fellowship from the Graduate Assistantships in Areas of National Need (GAANN) program of the US Department of Education.

References

Aussillous, B., Quere, D., 2002. Bubbles creeping in a viscous liquid along a slightly inclined plane. Europhys. Lett. 59, 370–376.

Blake, J.R., 1971. A note on the image system for a Stokeslet in a no-slip boundary. Proc. Cam. Phil. Soc.-Math. Phys. Sci. 70, 303.

Chen, K.H., Keh, P.Y., 2001. Slow motion of a droplet between two parallel walls. Chem. Eng. Sci. 56, 6863–6871.

DeBisschop, K.M., Miksis, M.J., Eckmann, D.M., 2002. Bubble rising in an inclined channel. Phys. Fluids 14, 93–106.

Griggs, A.J., Zinchenko, A.Z., Davis, R.H., 2006. The low-Reynolds-number motion of a deformable drop between two parallel plane walls. Int. J. Multiphase Flow 33, 182–206.

Hodges, S.R., Jensen, O.E., Rallison, J.M., 2004. Sliding, slipping, and rolling; the sedimentation of a viscous drop down a gently inclined plane. J. Fluid Mech. 512, 95–131.

Kim, S., Karrila, S.J., 1991. Microhydrodynamics: Principles and Selected Applications. Butterworths-Heinemann, Boston, MA.

Mortazavi, S., Tryggvason, G., 2000. A numerical study of the motion of drops in Poiseuille flow. Part 1. Lateral migration of one drop. J. Fluid Mech. 411, 325–350.

Rallison, J.M., Acrivos, A., 1978. A numerical study of the deformation and burst of a viscous drop in an extensional flow. J. Fluid Mech. 89, 191–200.

Richard, D., Quere, D., 1999. Viscous drops rolling on a tilted non-wettable solid. Europhys. Lett. 48, 286–291.

Stone, H.A., Bentley, B.J., Leal, L.G., 1986. An experimental study of the transient effects in the breakup of viscous drops. J. Fluid Mech. 173, 131–158.

Tsao, H., Koch, D.L., 1997. Observations of high Reynolds number bubbles interacting with a rigid wall. Phys. Fluids 9, 44–56.

Zinchenko, A.Z., Davis, R.H., 2000. An efficient algorithm for hydrodynamical interaction of many deformable drops. J. Comp. Phys. 157, 539–587.

Zinchenko, A.Z., Davis, R.H., 2005. A multipole-accelerated algorithm for close interaction of slightly deformable drops. J. Comp. Phys. 207, 695–735.

Zinchenko, A.Z., Davis, R.H., 2006. A boundary-integral study of a drop squeezing through interparticle constrictions. J. Fluid Mech. 564, 227–266.

Zinchenko, A.Z., Rother, M.A., Davis, R.H., 1997. A novel boundary-integral algorithm for viscous interaction of deformable drops. Phys. Fluids 9, 1493–1511.

Zinchenko, A.Z., Rother, M.A., Davis, R.H., 1999. Cusping, capture, and breakup of interacting drops by a curvatureless boundary-integral algorithm. J. Fluid Mech. 391, 249–291.